JTTEE5 16:690–697
DOI: 10.1007/s11666-007-9078-8
1059-9630/$19.00 © ASM International

Modeling of an Inductively Coupled Plasma for the Synthesis of Nanoparticles

Rodolphe Bolot, Christian Coddet, Cornelis Schreuders, Marc Leparoux, and Stephan Siegmann

(Submitted March 6, 2007; in revised form June 1, 2007)

Among other methods, inductively coupled plasma (ICP) torches can be used for the synthesis of nanoparticles. In this process, the precursor material is vaporized in the first step in the plasma core. In the second step, nucleation and condensation occur in the synthesis chamber where the plasma gets colder and high-purity nanoparticles are synthesized, the growth of which is stopped by gas quenching. From their low velocity and high temperature, induction plasmas are particularly adapted for this application. Numerical modeling is a good way to achieve a better knowledge and understanding of the process since non-intrusive diagnostics are fairly difficult to implement. In the present article, a two-dimensional model of an ICP torch was developed and validated on the basis of comparisons with data obtained by some other authors. Finally, the current frequency (13.56 MHz), pressure level (0.04 MPa), and gas flow rates were adjusted for the specific conditions of nanoparticles synthesis.

Keywords CFD modeling, ICP plasmas, nanoparticle synthesis

1. Introduction

Nanoparticles show novel properties compared to the bulk material with the same chemistry. The small size is responsible for many changes in the thermo-physical properties. Thus, there was an increasing interest in nanomaterials since the past five years.

High-frequency inductively coupled plasmas (ICP) (Ref 1-5) and direct current plasmas (Ref 6, 7) are used for a little less than 20 years for the synthesis of nanoparticles. The precursor material (powder) is first vaporized in the plasma core. Nucleation and aggregation take place downstream in the synthesis chamber in which the nanoparticle growth is stopped by gas quenching. Nowadays, this process is experimentally perfectible but understanding of the mechanisms has become essential in order to consider the influence of the different operating parameters and control the process more efficiently.

This article is an invited paper selected from presentations at the 2007 International Thermal Spray Conference and has been expanded from the original presentation. It is simultaneously published in *Global Coating Solutions, Proceedings of the 2007 International Thermal Spray Conference*, Beijing, China, May 14-16, 2007, Basil R. Marple, Margaret M. Hyland, Yuk-Chiu Lau, Chang-Jiu Li, Rogerio S. Lima, and Ghislain Montavon, Ed., ASM International, Materials Park, OH, 2007.

Rodolphe Bolot and **Christian Coddet,** LERMPS, University of Technology of Belfort-Montbéliard, Belfort Cedex, France; and **Cornelis Schreuders**, **Marc Leparoux**, and **Stephan Siegmann,** EMPA – Materials Science and Technology, Thun, Switzerland. Contact e-mail: rodolphe.bolot@utbm.fr.

Accordingly, numerical modeling was proved to be particularly adapted: computational fluid dynamic (CFD) permits to estimate the temperature and velocity fields in and outside the ICP torch (Ref 3-5, 8-20). In the present article, a two-dimensional axisymmetric model of the induction plasma was developed and used. The model represents the coupling between Navier-Stokes and extended-field electromagnetic equations formulated in terms of vector potential. The model validation was first performed on the basis of comparisons with results obtained by some other authors. Then it was used to model the ICP under the nanoparticle synthesis conditions.

2. Computational Fluid Dynamic Model

The interest for the modeling of high-frequency induction plasmas is about 30 years old. The model described by Boulos (Ref 8) in 1976 was based on a one-dimensional electromagnetic field model. Models expressed in terms of vector potential (Ref 9) are somewhat more recent. According to this model type, the electromagnetic coupling is considered using two conservation equations for the real and imaginary parts of the tangential component of the vector potential.

The use of an extended-field model was suggested much more recently (Ref 11). In this model, the vector potential equations are solved in an extended domain comprising the plasma region, the plasma confinement tubes, the induction coils themselves, and the external domain. It allows taking the coil design into account more accurately. At present, high-performance computers permit to carry out three-dimensional studies making it possible to consider the plasma dissymmetry generated by the coil (Ref 12, 13). Moreover, because the central gas is given a swirl component, it must be considered as suggested by Shigeta et al. (Ref 14-17).

In the present study, a two-dimensional model quite similar to that of Xue et al. (Ref 11) was developed but an additional equation was incorporated for the swirl component. In fact, taking the plasma dissymmetry into account is not our priority until now.

2.1 CFD Equations

Because the FLUENT (release 6.2.16) software (Lebanon, NH, USA) was used to implement the present model, the Navier-Stokes equations do not require any special consideration since they are integrated in the solver.

Thus, only the Lorentz forces (F_{Lx} and F_{Lr} components), ohmic heating (Q_J), and radiative loss (Q_R) terms must be taken into account by using adequate User-Defined Functions written in C language. Moreover, the default energy equation (expressed in terms of temperature within FLUENT) was deactivated and replaced by a scalar for enthalpy h. This change was performed in order to overcome the limited formula available within FLUENT for the specific heat, that must be integrated in the case of a temperature formulation.

In the case of a two-dimensional axisymmetric coordinate system (x, r, θ), the conservation equations may be written as:

- Continuity:

$$\frac{\partial(\rho u)}{\partial x}+\frac{1}{r}\frac{\partial(r\rho v)}{\partial r}=0 \qquad \text{(Eq 1)}$$

- Axial momentum:

$$\frac{\partial(\rho u^2)}{\partial x}+\frac{1}{r}\frac{\partial(r\rho uv)}{\partial r}-\frac{\partial}{\partial x}\left(\mu\frac{\partial u}{\partial x}\right)-\frac{1}{r}\frac{\partial}{\partial r}\left(r\mu\frac{\partial u}{\partial r}\right)=-\frac{\partial P}{\partial x}+\frac{\partial}{\partial x}\left(\mu\frac{\partial u}{\partial x}\right)+\frac{1}{r}\frac{\partial}{\partial r}\left(r\mu\frac{\partial v}{\partial x}\right)+F_{Lx} \qquad \text{(Eq 2)}$$

- Radial momentum:

$$\frac{\partial(\rho uv)}{\partial x}+\frac{1}{r}\frac{\partial(r\rho v^2)}{\partial r}-\frac{\partial}{\partial x}\left(\mu\frac{\partial v}{\partial x}\right)-\frac{1}{r}\frac{\partial}{\partial r}\left(r\mu\frac{\partial v}{\partial r}\right)=-\frac{\partial P}{\partial r}+\frac{\partial}{\partial x}\left(\mu\frac{\partial u}{\partial r}\right)+\frac{1}{r}\frac{\partial}{\partial r}\left(r\mu\frac{\partial v}{\partial r}\right)-2\mu\frac{v}{r^2}+\rho\frac{\omega^2}{r}+F_{Lr} \qquad \text{(Eq 3)}$$

- Swirl momentum:

$$\frac{\partial(\rho u\omega)}{\partial x}+\frac{1}{r}\frac{\partial(r\rho v\omega)}{\partial r}-\frac{\partial}{\partial x}\left(\mu\frac{\partial \omega}{\partial x}\right)-\frac{1}{r}\frac{\partial}{\partial r}\left(r\mu\frac{\partial \omega}{\partial r}\right)=-\frac{\omega}{r}\left(\rho v+\frac{\partial \mu}{\partial r}+\frac{\mu}{r}\right) \qquad \text{(Eq 4)}$$

- Enthalpy:

$$\frac{\partial(\rho uh)}{\partial x}+\frac{1}{r}\frac{\partial(r\rho vh)}{\partial r}-\frac{\partial}{\partial x}\left(\frac{\kappa}{Cp}\frac{\partial h}{\partial x}\right)-\frac{1}{r}\frac{\partial}{\partial r}\left(r\frac{\kappa}{Cp}\frac{\partial h}{\partial r}\right)=Q_J-Q_R \qquad \text{(Eq 5)}$$

in which ρ, μ, κ, and Cp stand for density, dynamic viscosity, thermal conductivity, and specific heat, respectively and u, v, and ω are the axial, radial, and swirl velocity components, respectively.

Concerning the electromagnetic coupling, the equations were formulated in terms of vector potential for which two additional scalars must be considered for the real and imaginary parts of the θ component of the vector. These equations may be written as follows:

$$-\frac{\partial^2 A_{\theta R}}{\partial x^2}-\frac{1}{r}\frac{\partial}{\partial r}\left(r\frac{\partial A_{\theta R}}{\partial r}\right)=S_{A_{\theta R}} \qquad \text{(Eq 6)}$$

$$-\frac{\partial^2 A_{\theta I}}{\partial x^2}-\frac{1}{r}\frac{\partial}{\partial r}\left(r\frac{\partial A_{\theta I}}{\partial r}\right)=S_{A_{\theta I}} \qquad \text{(Eq 7)}$$

where $A_{\theta R}$ and $A_{\theta I}$ are the real and imaginary parts of the θ component of the magnetic vector potential.

In the plasma, the source terms are expressed as:

$$S_{A_{\theta R}}=\omega\mu_0\sigma A_{\theta I}-\frac{1}{r^2}A_{\theta R} \quad \text{and} \quad S_{A_{\theta I}}=-\omega\mu_0\sigma A_{\theta R}-\frac{1}{r^2}A_{\theta I}$$

whereas in the inductor they are written as follows:

$$S_{A_{\theta R}}=\mu_0 J_{\text{coil}}-\frac{1}{r^2}A_{\theta R} \quad \text{and} \quad S_{A_{\theta I}}=-\frac{1}{r^2}A_{\theta I}.$$

Anywhere else, there in no electric current source so that:

$$S_{A_{\theta R}}=-\frac{1}{r^2}A_{\theta R} \quad \text{and} \quad S_{A_{\theta I}}=-\frac{1}{r^2}A_{\theta I}.$$

In these equations, $\omega=2\pi f$ where f is the induction current frequency (Hz), $\mu_0=4\pi\times10^{-7}$ H/m (or N/A^2) is the permeability of free space, σ is the electrical conductivity (S/m), and $J_{\text{coil}}=I_{\text{coil}}/S_{\text{coil}}$ is the electric current density (A/m^2) in the coil (I_{coil} is the coil current (A) and S_{coil} the coil cross-section (m^2)).

In the present model, the source term linearization was performed using:

$$dS_{A_{\theta R}}/dA_{\theta R}=-1/r^2 \quad \text{and} \quad dS_{A_{\theta I}}/dA_{\theta I}=-1/r^2$$

This permits to consider a part of the source terms implicitly. For example, in the case of $S_{A_{\theta R}}$, the second part of the source term $A_{\theta R}/r^2$ is transferred in the left-hand side of the linear equation written for $A_{\theta R}$, thus improving the stability of the solving procedure.

The magnetic fields may be obtained from the Maxwell equations as follows:

$$E_\theta=-i\omega A_\theta \quad \text{where } i^2=-1$$

$$\mu_0 H_x=\frac{1}{r}\frac{\partial}{\partial r}(rA_\theta) \quad \text{and} \quad \mu_0 H_r=-\frac{\partial A_\theta}{\partial x}$$

The Lorentz forces applied to the momentum equations may be written as:

$$F_{Lx}=-\frac{1}{2}\mu_0\sigma\text{Re}(E_\theta\bar{H}_r) \qquad \text{(Eq 8)}$$

and

$$F_{Lr}=\frac{1}{2}\mu_0\sigma\text{Re}(E_\theta\bar{H}_x) \qquad \text{(Eq 9)}$$

in which $\text{Re}(z)$ refers to the real part the z complex number and $\bar{z}$ is the conjugate complex number. For the ohmic production term, it comes that:

$$Q_J = \frac{1}{2}\sigma(E_\theta \bar{E}_\theta) \quad \text{(Eq 10)}$$

Thermodynamic and transport properties of thermal plasmas were estimated using the code developed in (Ref 21). This code was now rewritten in FORTRAN language. It uses a Gibbs free energy minimization method to compute the chemical equilibrium composition of any plasma mixture (Ar, He, H_2, N_2, O_2) versus temperature and pressure. It also permits to determine enthalpy, specific heat, thermodynamic derivatives, viscosity as well as thermal and electrical conductivities. All these data are tabulated in ASCII or binary files versus temperature at a given pressure. Under FLUENT, the so generated file may easily be reloaded using a user defined function written in C language.

Concerning the radiative loss term Q_R, in the case of a pure argon plasma at atmospheric pressure, the correlation suggested by Miller and Ayen already used by Boulos in 1976 (Ref 8) is still often considered in the literature as for example in the paper by Bernardi et al. (Ref 18). According to this correlation, the radiative loss term may be estimated from:

$$Q_R = 5600(T - 9500) + 181(T - 9500)^2 \quad \text{(Eq 11)}$$

where T in the temperature in K ($T > 9500$ K) and Q_R is the radiative loss term in W/m^3.

An alternative approach consists in using the correlation suggested by Wilbers et al. (Ref 22) that provides the radiative loss term (W/m/sr) versus electron density and temperature. This method was more suitable in the present study because it remains valid at any pressure level without further simplification. Moreover, it was easy to use in the present study because the electron density may be accessed in the plasma data file. Moreover, the radiative loss term being not available for each plasma mixture, the correlation provided by Wilbers et al. may represent a first approximation for any mixture for which this term is not available by assuming that the radiative loss term depends only on the electron density and temperature. However, metal vapors are known to affect significantly the radiative loss term as noticed by Essoltani et al. (Ref 23-26).

2.2 Model Validation

The model validation was performed on the basis of comparisons with numerical results obtained by Xue et al. (Ref 11). Thus, similar conditions were considered: the plasma torch was a PL50 model from TEKNA (Sherbrooke, QC, Canada), the design of which was described more precisely by Xue et al. The plasma confinement tube is 200 mm long and presents an internal diameter of 50 mm. The three turn coil presents a diameter of 66 mm. Two coaxial quartz tubes positioned in the main tube define three different inlet regions. The carrier gas is injected axially through the central tube, the central gas is injected between the central and intermediate cylinders with a swirl component and the sheath gas is injected along the plasma confinement tube. In the considered case, pure argon was used for each gas with flow rates of 1, 3, and 31 slpm for the carrier gas, the central gas, and the sheath gas, respectively.

Figure 1 presents the real and imaginary parts of the θ component of the magnetic vector potential (Ref 19). The fields and maximum values are very similar to the results obtained by Xue et al. (Ref 11).

The frequency of the generator was 3 MHz and the coil current intensity was adjusted at 170 A to provide a thermal power (integration of Q_J over the plasma volume) of

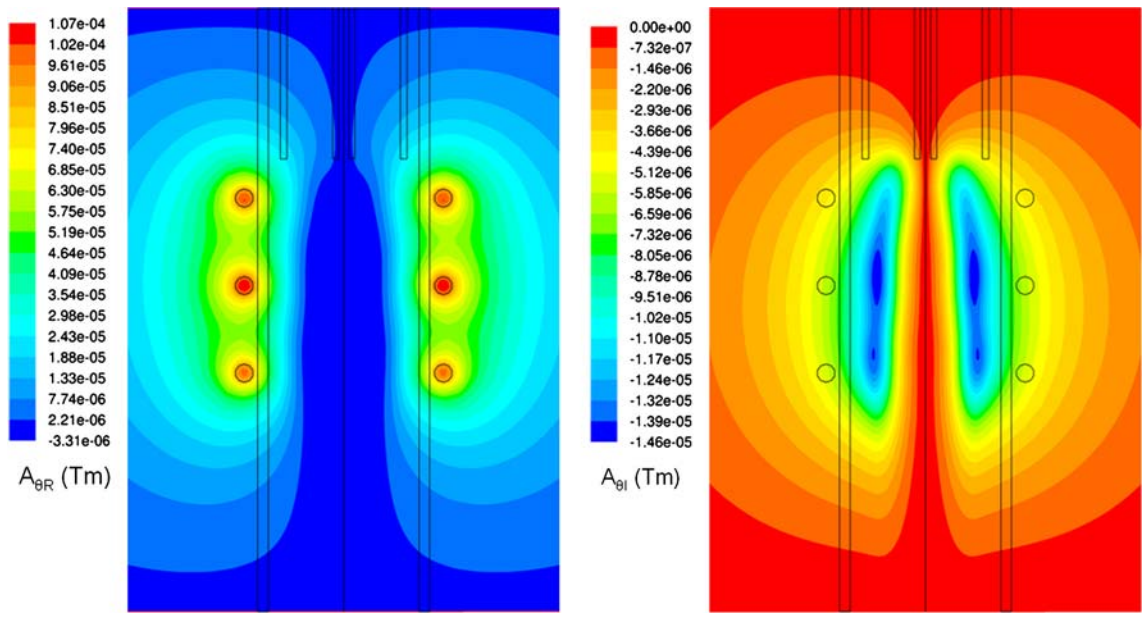

Fig. 1 Real and imaginary parts of the θ component of the magnetic vector potential

5 kW. This value is not really different from that indicated by Xue et al. (161 A) and the small gap between the two values may certainly be explained by some differences in the properties of the plasma (such as the electrical conductivity). For this validation step, the correlation of Miller and Ayen (Eq 11) was used to estimate the radiative loss term. Moreover, the injection of the central gas was performed through the whole area comprised between the central cylinder and the intermediate one and the swirl injection was not taken into account (the swirl momentum equation was not considered).

Figure 2 presents the fields of the axial velocity component, temperature, and ohmic heating term. The maximum value of the velocity is 17.5 m/s and that of the temperature is a little bit less than 9900 K. A good agreement was found again with the results obtained by Xue et al. and this is also the case for the heat production term for which a maximum value of 0.143 W/mm^3 was noted in (Ref 19). Finally, all the results obtained in the present test case tend to confirm the validity of the developed model. One can also notice the presence of a backflow region just at the exit of the carrier gas injector from the electromagnetic phenomena.

2.3 Nanoparticle Synthesis

The conditions used at EMPA for the synthesis of nanoparticles are somewhat different from that studied just above. In particular, a PL35-type torch incorporating ceramic tubes instead of quartz tubes is preferably used and higher gas flow rates are considered with a higher current frequency and a higher thermal power. The PL35 torch presents a smaller inner diameter (i.e., 35 mm instead of 50) and a 100 mm long plasma confinement tube. A 27 mm long additional part positioned upstream was considered in order to take the real positioning of the carrier and central gases injection points into account. Moreover, a 13 mm long part was added downstream in order to consider the presence of a convergent placed just at the torch exit (minimum diameter 30 mm).

The four turn coil has a diameter of 52 mm and extends over a length of 45 mm. The beginning of the first turn of the coil is positioned axially just at the exit of the central and intermediate tubes. However, in our two-dimensional axisymmetric model, the four turn coil was represented by four rings. Thus, the first ring was positioned axially at 5.6 mm from the exit of the interior cylinders, corresponding to the mean position of the first turn of the coil. In practice, the central gas is injected through eight holes (1 mm internal diameter) with a swirl component. Concerning the two-dimensional axisymmetric model, a 1 mm high annular section leveling the interior of the intermediate ceramic tube was considered for the central gas injection region. Moreover, a swirl component calculated in order to produce the real swirl momentum was given to the central gas. Figure 3 presents the torch geometry of

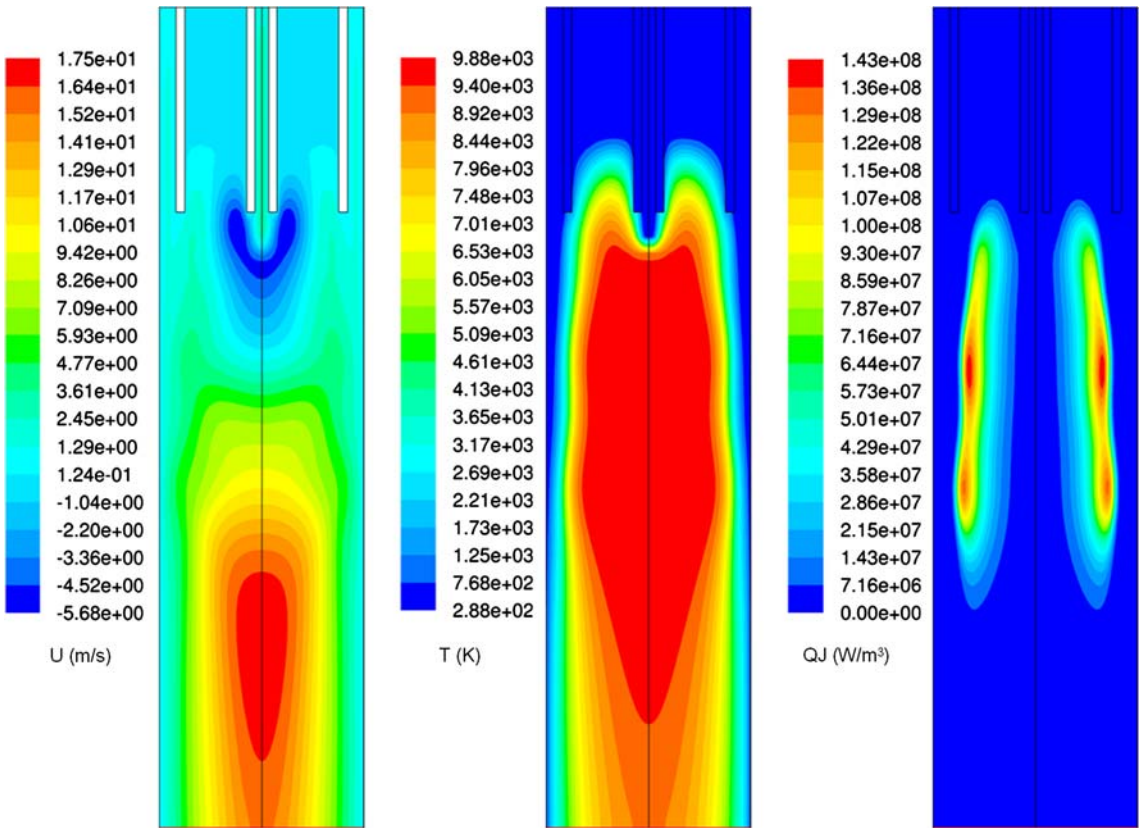

Fig. 2 Fields of axial velocity, temperature, and heat production term

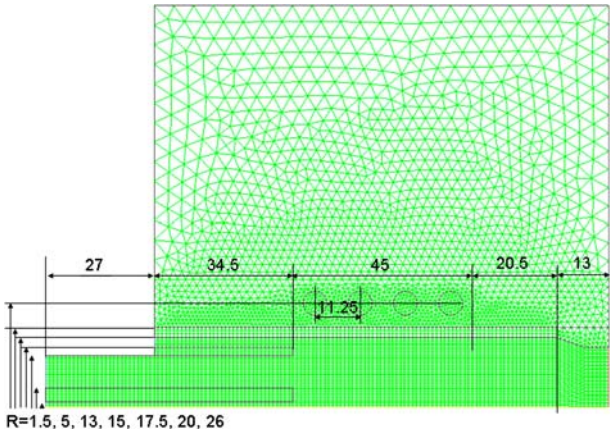

Fig. 3 Design of the PL35 torch and grid

the PL35 torch and the grid used in the present study. The mesh was formed by rectangular cells in the plasma region and in the solid cylinders and by triangular cells in the rings and in the external domain.

The case studied in the following concerns typical parameters used at EMPA for the synthesis of nanoparticles. The carrier gas and central gas flow rates are set to 3 and 12 slpm of pure argon, respectively, whereas the sheath gas is composed of 80 slpm of argon and 6 slpm of hydrogen. A supplementary conservation equation was added for the mass fraction of sheath gas and the diffusion coefficient for this equation was estimated on the basis of a unitary Lewis number assumption ($\rho D = \kappa/Cp$). The plasma properties are then interpolated versus the local mass fraction of each gas mixture. The working pressure was 40 kPa instead of 101 kPa. Moreover, because of the lack of data concerning radiative losses of argon/hydrogen plasmas, the correlation proposed by Wilbers et al. was used to estimate the radiative loss term although it concerns pure argon. Nevertheless, the contribution of radiative losses is much lower at 0.04 MPa in comparison with the 0.1 MPa case, so that one can expect that this assumption has no strong influence on the numerical predictions.

The high-frequency generator provides a current frequency of 13.56 MHz instead of 3 MHz for the test case described previously. Moreover, the coil current was set to 118 A in order to give an ohmic heating power of 12 kW (numerical integration of Q_J over the plasma volume). According to the predictions, only 1.35 kW are lost by radiations (numerical integration of Q_R over the plasma volume). Thus the radiative losses represent about 11% of the ohmic heating power at 0.04 MPa, but this fraction is more important at 0.1 MPa.

Figure 4 presents the fields of the swirl and axial components of the velocity, and temperature. One may notice that the velocity is much higher in the present case in comparison with the test case. This major difference is provided by different changes:

- decrease of the torch diameter from 50 to 35 mm,
- presence of a convergent nozzle,
- increase of all gas flow rates and of the thermal power from 5 to 12 kW, and
- decrease of the pressure level from 0.1 to 0.04 MPa.

From the different operating conditions, the axial velocity component is about ten times higher (180 m/s instead of 17.5) for the present results in comparison with the former case. The swirl component reaches its maximum value of 60 m/s in the central gas injection region. In fact, the swirl component permits to stabilize the plasma in the torch. According to the numerical results, the plasma would be blown outside the torch if the swirl component is not taken into account. Thus, although the swirl component was found to have only a small effect in the previous test case (PL50 low-velocity case), it seems to have a major role in the present range of parameters (PL35, high gas flow rates, low pressure, etc.). One can also notice that the negative velocity region found at the exit of the carrier gas injection tube disappeared for the new conditions. This may have a positive effect on the precursor powder that will flow axially without any recirculation risk (especially for the smallest particles). However, the backflow region situated along the external face of the powder injection tube is still present for the new conditions.

Concerning the temperature field, the maximum temperature (a little bit lower than 11,000 K) is higher than that obtained for the former case and the contours look different. In particular, the plasma seems disrupted by the axial injection of the carrier gas, providing a cold region along the torch axis (Ref 19) and giving the plasma an annular shape. Moreover, this effect increases with the increase in the carrier gas flow rate.

3. Experimental Results

In practice, the plasma jet formed at the torch exit for the conditions of Fig. 4 discharges in the synthesis chamber (diameter 320 mm) after two successive enlargements (diameter of 70 mm over an axial distance of 23 mm and diameter of 85 mm over a distance of 10 mm). In the synthesis chamber, nucleation takes place where the plasma gets colder and nanoparticle agglomerates are formed by coagulation. The process is stopped by gas quenching at an axial distance of about 100 mm from the torch exit represented in Fig. 4. Figure 5 presents the reactor prototype (left side of the photo) developed at the EMPA of Thun (filter on the right side). The plasma torch is situated in the top part of the reactor.

Figure 6 presents two views of the RF plasma observed inside the chamber with a mirror. The green color is caused by the presence of a filter placed to reduce the light intensity. The left picture concerns a low carrier gas flow rate case (flow rates of 1 ,12, and 80+6 slpm for the carrier gas, central gas, and sheath gas, respectively) whereas the right picture concerns a high carrier gas flow rate (10 slpm instead of 1). The operating pressure was 60 kPa in each case. As it could be expected from numerical results, experiments show that the plasma is disrupted by the

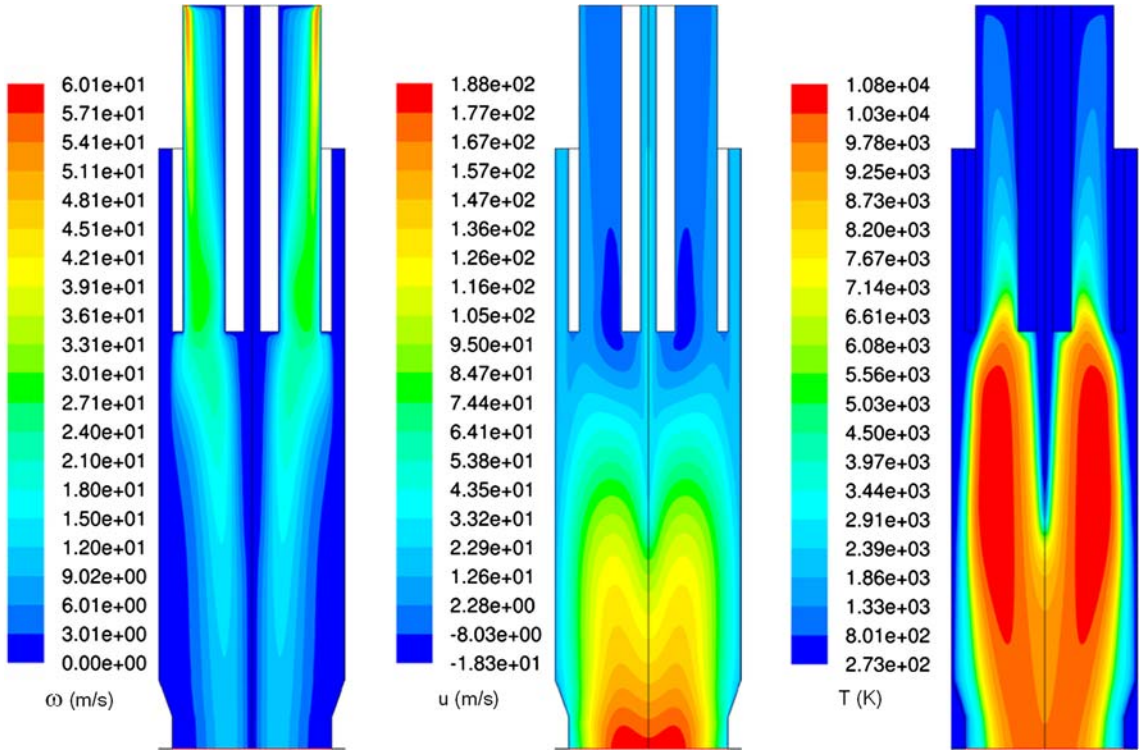

Fig. 4 Swirl (left) and axial (center) velocity component fields and temperature field (right)

Fig. 5 Reactor prototype developed at the EMPA of Thun for the synthesis of nanoparticles (Ref 27)

carrier gas injection and this effect increases with the increase in the carrier flow rate.

Figure 7 presents a few nanoparticles of Silicon elaborated in the experimental device depicted in Fig. 5 with the parameters modeled in the latter case (3-12-80/6 slpm at 40 kPa). The initial feedstock particle size distribution was +44-16 μm and a powder flow rate of 1.9 g/min was used. The nanoparticle growth was stopped by using a quenching device composed of a ring with a 64 mm diameter equipped with eight nozzles inclined with an

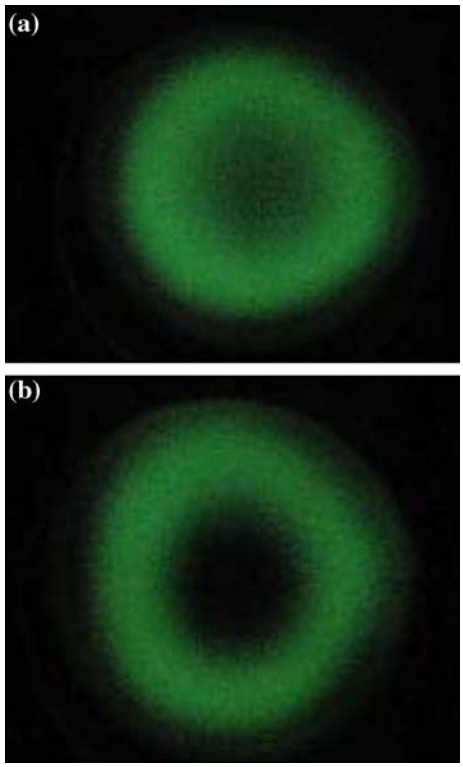

Fig. 6 Views of the plasma observed using a mirror. Parameters 1-12-80/6 slpm (a) and 10-12-80/6 slpm (b) – $P = 0.06$ MPa

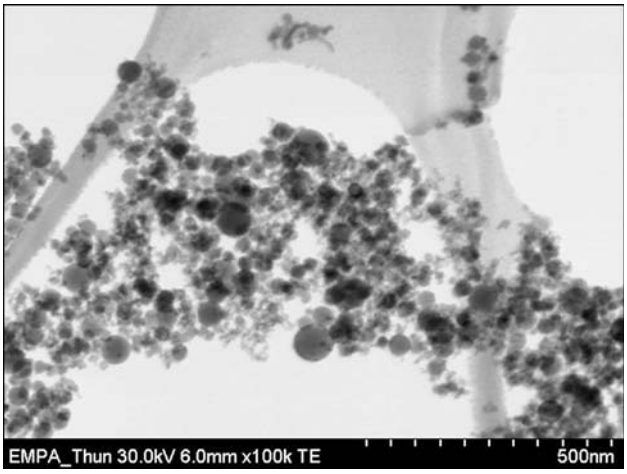

Fig. 7 Si nanoparticles collected near the filter. Parameters 3-12-80/6 slpm – $P = 0.04$ MPa

angle of 15° in the direction of the plasma flow. This device was placed at a distance of 122 mm from the torch exit represented in Fig. 4 and a quenching gas flow rate of 56 slpm was used. Moreover, a funnel was placed over the quenching device in order to avoid that the plasma goes round it. The nanoparticles were collected near the filter.

4. Conclusion

A CFD model of a high-frequency ICP was developed in order to obtain a better knowledge and understanding of the nanoparticle synthesis process used at the EMPA of Thun (Switzerland). This model considers the coupling between electromagnetic and Navier-Stokes equations and was implemented in the FLUENT software by using User Defined Functions (UDFs) written in C language. The contribution of the magnetic part was formulated in terms of vector potential on the basis of a two-dimensional axisymmetric assumption and an extended field of calculation was considered. The model permits to quantify the influence of the more relevant parameters such as the gas flow rates, the current frequency, the working pressure, the power input, etc. on the plasma flow and on the main characteristic fields such as velocity and temperature. According to the model, the swirl flow permits to stabilize the plasma in the torch and must hence be taken into account. In a next step, the calculation domain will be extended to the downstream (i.e., synthesis chamber) region. The initial powder evaporation will be considered and the nanoparticle formation and growth will be modeled.

References

1. S.L. Girshick and C.P. Chiu, Homogenous Nucleation of Particles from the Vapor Phase in Thermal Plasma Synthesis, *Plasma Chem. Plasma Process.*, 1989, **9**(3), p 355-359
2. S.L. Girshick, C.P. Chiu, R. Muno, C.Y. Wu, L. Yang, S.K. Sing, and P.H. McMurry, Thermal Plasma Synthesis of Ultrafine Iron Particles, *J. Aerosol Sci.*, 1993, **24**(3), p 367-382
3. P. Proulx and J.-F. Bilodeau, A Model for Ultrafine Powder Production in a Plasma Reactor, *Plasma Chem. Plasma Process.*, 1991, **11**(3), p 371-386
4. J.-F. Bilodeau and P. Proulx, A Mathematical Model for Ultrafine Iron Powder Growth in a Thermal Plasma, *Aerosol Sci. Technol.*, 1996, **24**, p 175-189
5. M. Desilets, J.-F. Bilodeau, and P. Proulx, Modelling of the Reactive Synthesis of Ultra-Fine Powders in a Thermal Plasma Reactor, *J. Phys. D: Appl. Phys.*, 1997, **30**, p 1951-1960
6. N. Rao, S. Girshick, J. Heberlein, P. McMurry, S. Jones, D. Hansen, and B. Micheel, Nanoparticle Formation Using a Plasma Expansion Process, *Plasma Chem. Plasma Process.*, 1995, **15**(4), p 581-606
7. N. Rao, B. Micheel, D. Hansen, C. Faudrey, M. Bench, S. Girshick, J. Heberlein, and P. McMurry, Synthesis of Nanophase Silicon, Carbon and Silicon Carbide Powders using a Plasma Expansion Process, *J. Mater. Res.*, 1995, **10**(8), p 2073-2084
8. M.I. Boulos, Flow Temperature Fields in the Fire-ball of an Inductively Coupled Plasma, *IEEE Trans. Plasma Sci.*, 1976, **4**, p 28-39
9. J. Mostaghimi and M.I. Boulos, Two-dimensional Electromagnetic Field Effects in Induction Plasma Modelling, *Plasma Chem. Plasma Process.*, 1989, **9**, p 25-44
10. B.W. Yu and S.L. Girshick, Modeling Inductively Coupled Plasmas: The Coil Current Boundary Condition, *J. Appl. Phys.*, 1991, **69**(2), p 656-661
11. S. Xue, P. Proulx, and M.I. Boulos, Extended-field Electromagnetic Model for Inductively Coupled Plasma, *J. Phys. D: Appl. Phys.*, 2001, **34**, p 1897-1906
12. D. Bernardi, V. Colombo, E. Ghedini, and A. Mentrelli, Three-dimensional Modelling of Inductively Coupled Plasma Torches, *Eur. Phys. J. D*, 2003, **22**, p 119-125
13. D. Bernardi, V. Colombo, E. Ghedini, and A. Mentrelli, Three-dimensional Effects in the Modelling of ICPTs – Part I: Fluid Dynamics and Electromagnetics, *Eur. Phys. J. D*, 2003, **25**, p 271-277
14. M. Shigeta, T. Sato, and H. Nishiyama, Numerical Simulation of Potassium-Seeded Turbulent RF Inductively Coupled Plasma with Particles, *Thin Solid Films*, 2003, **435**, p 5-12
15. M. Shigeta, T. Sato, and H. Nishiyama, Computational Simulation of Particle-laden RF Inductively Coupled Plasma with Seeded Potassium, *Int. J. Heat Mass Transfer*, 2004, **47**, p 707-716
16. M. Shigeta, T. Watanabe, and H. Nishiyama, Numerical Investigation of Nanoparticle Synthesis in an RF Inductively Coupled Plasma, *Thin Solid Films*, 2004, **457**, p 192-200
17. M. Shigeta and H. Nishiyama, Numerical Analysis of Metallic Nanoparticle Synthesis using RF Inductively Coupled Plasma Flows, *J. Heat Transfer*, 2005, **127**, p 1222-1230
18. D. Bernardi, V. Colombo, E. Ghedini, and A. Mentrelli, Comparison of Different Techniques for the FLUENT-based Treatment of the Electromagnetic Field in Inductively Coupled Plasma Torches, *Eur. Phys. J. D*, 2003, **27**, p 55-72
19. R. Bolot, C. Schreuders, M. Leparoux, S. Siegmann, and C. Coddet, Modélisation de la synthèse de nanoparticules par plasma d'induction haute fréquence (Modeling of Nanoparticle Synthesis with a High Frequency Inductively Coupled Plasma), *Proc. of MATERIAUX 2006*, November 13-17, Dijon, France (in French)
20. B.M. Goortani, P. Proulx, S. Xue, and N.Y. Mendoza-Gonzalez, Controlling Nanostructure in Thermal Plasma Processing: Moving from Highly Aggregated Porous Structure to Spherical Silica Nanoparticles, *Powder Technol.*, 2007, **175**, in press
21. R. Bolot, ''Modélisation des plasmas d'arc soufflé : Application à la projection de matériaux pulvérulents (Modeling of Blown Arc Plasmas – Application to Thermal Spray of Powders),'' PhD thesis, Université de Franche-Comté, France, 1999 (in French)
22. A.T.M. Wilbers, J.J. Beulens, and D.C. Schram, Radiative Energy Loss in a Two-Temperature Argon Plasma, *J. Quant. Spectrosc. Radiat. Transfer*, 1991, **46**, p 385-392
23. A. Essoltani, P. Proulx, M.I. Boulos, and A. Gleizes, Radiation and Self-absorption in Argon – Iron Plasmas at Atmospheric Pressure, *J. Anal. Atomic Spectrosc.*, 1990, **5**, p 543-547

24. P. Proulx, J. Mostaghimi, and M.I. Boulos, Radiative Energy Transfer in Induction Plasma Modelling, *Int. J. Heat Mass Transfer*, 1991, **34**(10), p 2571-2579
25. A. Essoltani, P. Proulx, M.I. Boulos, and A. Gleizes, Effect of the Pressure of Iron Vapors on the Volumetric Emission of Ar/Fe and Ar/Fe/H Plasmas, *Plasma Chem. Plasma Process.*, 1994, **14**(3), p 301-315
26. A. Essoltani, P. Proulx, M.I. Boulos, and A. Gleizes, Volumetric Emission of Argon Plasmas in the Presence of Vapors of Fe, Si, and AI, *Plasma Chem. Plasma Process.*, 1994, **14**(4), p 437-450
27. M. Leparoux, C. Schreuders, J.W. Shin, and S. Siegmann, Induction Plasma Synthesis of Carbide Nanopowders, *Adv. Eng. Mater.*, 2005, **7**, p 349-353